Nanoscale

PAPER

View Article Online
View Journal

Cite this: DOI: 10.1039/d5nr04595a

Aggregation-induced emission active seminaphthofluoresceins: a new class of xanthene luminogens for bioimaging

Laura McKay, [a] Issan Zhang, [b] Imogen Suh,[a] D. Scott Bohle, [a] Ashok Kakkar *[a] and Dusica Maysinger *[b]

The development of aggregation-induced emission (AIE) luminogens has made marked and diverse impacts in the areas of bioimaging and theragnostics. While virtually every class of traditional aggregation-caused quenching (ACQ) fluorophores have been investigated for the purposes of establishing the sought after ACQ to AIE transformation, the prolific xanthene family has remained largely overlooked. A recent brief report of simple derivatized fluoresceins exhibiting AIE characteristics upended the prevailing perception of fluoresceins as fixed ACQ species but limited progress has taken place in the years following. In this study we take the first step towards highly functional xanthene AIEgens, exploring both the nuances of aggregation and translation to applications in imaging and sensing. The synthetic modification of seminaphthofluoresceins (benzo[*c*]xanthenes, π-extended fluorescein derivatives) yields luminogens exhibiting high Stokes shifts, bathochromically shifted emission, and aggregation-induced emission behaviour. The optical properties of the seminaphthofluorescein propargyl ethers, possessing terminal alkyne moieties for facile customization, are assessed both in the dissolved state and throughout the aggregation process. As a result of their controlled response to non-solvents over a broad range of solution compositions, the luminogens are suited for the optical sensing of water content in organic solvents. The aggregates were utilized for organelle imaging in microglia, the immune cells of the brain, and accumulated predominantly in the mitochondria. When coupled with their limited reliance on membrane potential, these findings suggest the luminogens as novel and versatile tools for intracellular visualization, tracking, and interactions of mitochondria with other organelles.

Received 30th October 2025,
Accepted 9th January 2026

DOI: 10.1039/d5nr04595a

rsc.li/nanoscale

1. Introduction

The xanthene family of fluorescent dyes (comprised broadly of fluoresceins, rhodols, and rhodamines) has remained ubiquitous for over 150 years, with chief applications in chemical biology and medicine.[1–3] Fluoresceins are an outstanding pillar of the class as a result of their exceptional quantum yields, low toxicity *in vivo*, and pH sensitivity.[4,5] As is the case for the vast majority of conventional organic fluorophores, xanthenes are known to experience aggregation-caused quenching (ACQ). ACQ is a fundamental photophysical concept describing the reduction or complete extinction of fluorescence upon aggregation of a fluorophore, at high concentrations in solution, in thin films, and the solid state.[6–9] The ACQ phenomenon places restrictive limits on the imaging applications of species which are subject to this process, requiring careful control of concentration and solubility, restricting both maximum brightness (by extension signal to noise ratios) and the utility of lipophilic compounds.[10–12] In 2001, Tang *et al.* transformed the landscape with their report of a weakly emitting pentaphenylsilole species undergoing a substantial increase in brightness upon aggregation.[13] While isolated cases of 'unusual' species evidently not impacted by ACQ previously existed in literature, Tang established both the term aggregation-induced emission (AIE) and a concrete pathway for further development through mechanistic understanding.[14,15] In the following years, the field has experienced extraordinary growth, with the unique properties of AIE active compounds ('lumino-gens/phores' or AIEgens) finding utility in a diverse range of applications, from diagnostic imaging to optoelectronics.[16–20]

In the specific context of biological imaging, the impact of AIE luminogens has been described as uniquely revolutionary.[21] Within the diverse environment of the cell, fluorophores are likely to encounter areas of spatial confinement and high concentration, inducing unfavourable interactions between

[a]*Department of Chemistry, McGill University, 801 Sherbrooke St. West, Montreal, Quebec H3A 0B8, Canada. E-mail: ashok.kakkar@mcgill.ca*
[b]*Department of Pharmacology and Therapeutics, McGill University, 3655 Promenade Sir-William-Osler, Montreal, Quebec, Canada H3G 1Y6. E-mail: dusica.maysinger@mcgill.ca*

chromophores and/or aggregation. Organelle specific probes are uniquely vulnerable to aggregation-caused quenching effects due to immense concentration enhancement within the targeted structure.[10,22,23] In the case of lipophilic cations with affinity for the mitochondria, this concentration enhancement factor can reach 500 fold.[24] As a result, commercial fluorophores utilized for organelle staining, including the MitoTracker series, are prone to signal loss and other aberrations linked to quenching. Similarly, the long-term monitoring of biological processes and cellular dynamics is limited by the progressive degradation and aggregation of conventional probes. While individual properties vary, aggregated AIE luminogens have largely been seen to exhibit impressive resistance to both photobleaching and degradation in the biological environment.[25–27] Beyond resolving the longstanding issue of ACQ, the development of AIE materials has pushed the boundaries of what constitutes high performance and functionality in imaging.

Extensive molecular engineering and synthetic efforts have yielded an impressive range of AIEgens and establishment of the ACQ to AIE transformation for nearly every class of conventional fluorophores.[28–33] Curiously, xanthenes have been largely excluded from this development, remaining concretely in the ACQ category. A key review by the Tang group presents the concepts of ACQ and AIE using striking photographs in which fluorescein is visualized as the model species for aggregation-caused quenching, likely further solidifying the general view of xanthenes as entirely separate from AIE development.[16] While a limited number of reports of hybrid systems exist, in which a traditional xanthene is linked to an AIE luminogen, these are not representative of a true ACQ to AIE transformation.[26,34–36] Of the wider xanthene class only rhodamines have begun to merge into the AIE domain, with a modest collection of synthetically complex derivatives demonstrating enhanced emission in the aggregate state.[37,38]

In 2020, nearly two decades after the onset of the AIE boom, Feng. *et al.* discovered that simple functionalization of the fluorescein skeleton resulted in enhanced emission from solution aggregates and strong solid-state luminescence.[39] Their brief investigation of these allyl ethers, unanticipated byproducts in the synthesis of materials for carbon monoxide detection, upended the conventional perception of fluoresceins and their potential for AIE. Despite strong interest in this work and clear promise of these unique luminogens, very little progress in this area has been made since the initial communication.[40] To date there has been no noteworthy expansion of the preliminary class, a key stage in the development and optimization of any given family of fluorophores. In addition, despite representing the first milestone in the translation of fluoresceins to the AIE domain, the luminogens had several drawbacks including high energy emission and low Stokes shifts which mimicked their parent fluoresceins.[4,5] Within the xanthene family, elongation of the π system through benzannulation has been well established as an effective strategy to induce significant bathochromic shifts and desirable Stokes shifts.[41,42] Asymmetric π-extended derivatives seminaphthofluoresceins (SNAFL) and seminaphthorhodafluors (SNARF), best known for their ratiometric pH sensing capability, are particularly promising.[43–46]

Herein we report the synthesis of seminaphthofluorescein propargyl ethers TPRP-SNAFL **1** and DPRP-SNAFL **2**, the first benzoxanthenes exhibiting aggregation-induced emission (Scheme 1). A detailed spectral and photophysical analysis of the species in organic solvent was used to establish baseline behaviour in the solution state. The dissolved luminogens are seen to retain several favourable properties of their seminaphthofluorescein parent compounds, including high Stokes shifts and redshifted emission. Aggregation was induced in binary organic–aqueous solutions, and the process was followed in detail by UV-Vis, fluorescence emission, and lifetime measurements. Aggregation of TPRP-SNAFL and DPRP-SNAFL led to increased extinction coefficients, fluorescence quantum yields, and extended lifetimes. A crystal structure was obtained to probe the mechanism of the ACQ to AIE transformation, revealing a lack of close face to face π stacking and a variety of intermolecular and intramolecular short-range interactions contributing to restriction of rotation. The effect of solvent choice on the aggregation process was examined in parallel with a focus on the exceptional effect of alcohols. Additionally, the controlled response of both compounds to the presence of water, the non-solvent triggering aggregation, enabled the luminogens to act as optical sensors for water content in organic solvents.

An initial evaluation of both luminogens for intracellular imaging applications, the first of its kind for fluorescein AIEgens, revealed strong uptake of the bare aggregates by microglia and unanticipated organelle localization. Despite the absence of established structural motifs for organelle targeting, the aggregates of compounds **1** and **2** demonstrated substantial mitochondrial localization. Organelle specific fluo-

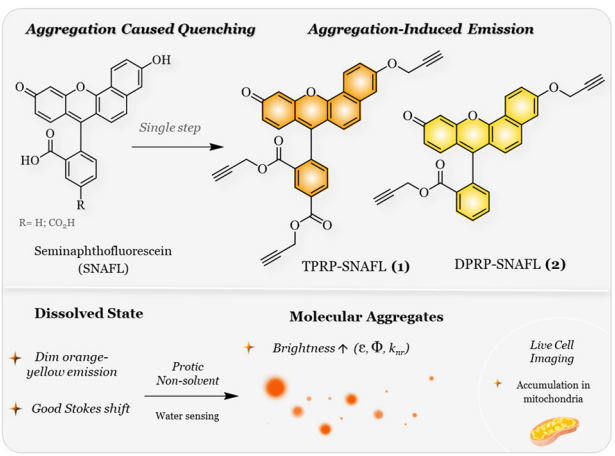

Scheme 1 Schematic diagram illustrating transformation of ACQ SNAFL fluorophores to AIE luminogens TPRP-SNAFL and DPRP-SNAFL with the formation of emissive nano-aggregates in protic non-solvents and their biological evaluation.

rescent markers are indispensable for the monitoring of cellular processes and organelle dynamics.[47–49] The development of mitochondria specific probes is a complex task nearly universally involving cationic species designed to exploit the characteristic negative potential across the inner mitochondrial membrane.[47,50,51] While there is an available wealth of knowledge about mitochondria in different cell types, relatively little is known about mitochondria in microglia which are exposed to AIE luminogens used for high contrast bioimaging.[21] In addition, understanding of the specific molecular mechanisms associated with mitochondrial dysfunction and the progression of neuroinflammation in neurodegenerative diseases remains limited. Mitochondrial dysfunction is associated with and likely causally related to numerous neurological disorders.[52–55] Microglial morphology, functions, and interactions between different organelles, including lipid droplets and lysosomes, play roles in the progression of neurological disorders.[56,57] Possible microglia-targeted interventions and treatments against neurodegenerative diseases with preclinical and clinical evidence in cell experiments, animal studies, and clinical trials are reviewed by Gao *et al.*[58] In this study, we demonstrate that uptake of fluorescent aggregates of both compounds in microglia could be successfully employed to visualize mitochondria. Collectively, this work represents a significant step towards concrete establishment of the ACQ to AIE conversion of xanthenes and in the direction of unique applications in bioimaging.

2. Experimental

2.1 Materials and instrumentation

Purified water was obtained from a Millipore Milli-Q (MQ) system. Reagents and solvents were purchased from Sigma Aldrich or Oakwood Chemical and used as received. Solvents for NMR analysis were purchased from Cambridge Isotope Laboratories and used as received. Column chromatography was performed using silica gel 60 (230–400 mesh) from Silicycle Inc. ^{1}H and ^{13}C NMR characterizations were performed on a Bruker AVIIIHD 500 MHz NMR Spectrometer. Atomic force microscopy data was acquired on a MFP3D AFM equipped with an molecular force probe controller (Asylum Research – Oxford Instruments, Santa Barbara, CA) in AC mode in air using ACTA probes (Applied Nanostructures, Inc., Mountain View, CA).

Chemical shifts (δ) are reported in parts per million (ppm) relative to tetramethylsilane using the residual solvent peak as a reference. UV-Vis absorption spectra were recorded on a Varian Cary 50 spectrophotometer and fluorescence measurements were carried out on an Agilent Cary Eclipse spectrophotometer. Fluorescence lifetimes were obtained with an Edinburg Instruments Mini-tau unit by time correlated single photon counting. Relative quantum yields are reported with reference to commercial rhodamine 101 by the following equation in which 's' and 'r' denote sample and reference, respectively. Concentrations were adjusted to keep absorbance at (and above) the excitation wavelength below 0.1 with differences in refractive index accounted for.

$$\Phi = \Phi_{\mathrm{r}}\left(\frac{m_{\mathrm{s}}}{m_{\mathrm{r}}}\right)\left(\frac{n_{\mathrm{s}}}{n_{\mathrm{r}}}\right)^{2}$$

2.2 Methods

General procedure – synthesis of luminogens 1 and 2. A general procedure for the synthesis of **1** and **2** is described here. Details and characterization are provided in the SI. A dry two neck round bottom flask charged with the appropriate seminaphthofluorescein was purged with nitrogen before the addition of HPLC grade acetone. Anhydrous potassium carbonate was added, followed by the slow addition of propargyl bromide by syringe. The reaction was heated to 60 °C and allowed to proceed under nitrogen flow for 48–85 h, during which time the hue of the mixture transitioned from a pale brown to deep purple. Solvent was removed under reduced pressure and the resulting solid was transferred to a separatory funnel with ethyl acetate and washed with portions of water and saturated brine. The organic solution was dried with magnesium sulfate before the solvent was removed to yield a foaming red-purple solid. The crude product was loaded onto a moderate length silica column and eluted with a methanol/dichloromethane solvent system, yielding the seminaphthofluorescein propargyl ether as a reflective red powder.

Preparation of binary solutions. Organic–aqueous solutions were prepared with consideration of non-additive volumes of mixtures of this nature.[59,60] In order to produce solutions with an accurate v/v% value, the aqueous component was pipetted first into the selected volumetric flask. The organic solvent was subsequently introduced dropwise with thorough mixing until the meniscus reached the mark. Final solutions were sealed and used within the hour to minimize risk of composition change.

Cell culture and treatments. Human HMC3 microglia were obtained from the American Type Culture Collection. Cells were cultured in Dulbecco's Modified Eagle Medium (DMEM, Gibco) supplemented with 5% (v/v) fetal bovine serum (Wisent) and 1% (v/v) penicillin–streptomycin (Gibco). Cells were kept at 37 °C in 5% CO_2 and 95% relative humidity. TPRP-SNAFL and DPRP-SNAFL were diluted in aqueous media from a 1 mM DMSO stock solution.

Time and concentration dependent cellular internalization. Cells were seeded on 12 mm diameter glass coverslips (Assistent) at 7000 cells per coverslip and cultured overnight. Cell nuclei were labelled with Hoechst 33342 (1 μM, 30 min). For time-dependent cellular internalization, cells were treated with 1 μM of compounds **1** or **2** for 5, 15, 30, or 45 min in phenol red-free Hank's Balanced Salt Solution (HBSS, Gibco) at 37 °C. Cells were rinsed in HBSS, then imaged using a fluorescence microscope (Leica DMI4000 B) at 63× magnification using the fluorescence filters DAPI-1160A (Semrock, ex: 387 nm, em: 447 nm) and TRITC-A (Semrock, ex: 542 nm, em: 620 nm). The relative fluorescence intensity per cell was analysed from fluorescence micrographs using ImageJ (version 1.54p). For con-

centration-dependent cellular internalization, cells were seeded at 7000 cells per well into a 96-well plate (Sarstedt) and cultured overnight. Cells were treated with 0.001, 0.05, 0.25, 0.5, 1, 5, 10 and 20 μM **1** or **2** for 24 h, after which the culture medium was removed, and cells were lysed in DMSO (100 μL per well). Lysate fluorescence was measured using a plate reader (Tecan Infinite M1000, ex: 542 nm, em: 620 nm).

Imaging of co-labelled mitochondria and lipid droplets. Cells were seeded on 12 mm diameter glass coverslips (Assistent) at 7000 cells per coverslip and cultured overnight. For mitochondrial imaging, cells were treated with **1** or **2** (1 μM) along with MitoTracker Deep Red FM (50 nM, Invitrogen) and Hoechst 33342 (1 μM) for 30 min in HBSS. For lipid droplet imaging, cells were treated with **1** or **2** (1 μM) along with BODIPY 493/503 (10 μM, Invitrogen) and Hoechst 33342 (1 μM) for 30 min in HBSS. Cells were rinsed in HBSS, then imaged using a fluorescence microscope at 63× magnification and the fluorescence filters DAPI-1160A, GFP-3035B (Semrock, ex: 472 nm, em: 520 nm), TRITC-A and CY5-404A (Semrock, ex: 628 nm em: 692 nm). Pearson's colocalization coefficients were calculated in ImageJ using Coloc 2.

Mitochondrial membrane potential. Cells were seeded on 12 mm diameter glass coverslips at 7000 cells per coverslip and cultured overnight. Cells were treated with **1**, **2**, or the mitochondrial membrane potential probe TMRE (Invitrogen) at 1 μM for 30 min at 37 °C in HBSS, with or without the mitochondrial uncoupler FCCP (20 μM, Sigma-Aldrich). Nuclei were labelled with Hoechst 33342 (1 μM) at the same time. Cells were rinsed in HBSS, then imaged using a fluorescence microscope (Leica DMI4000 B) at 63× magnification using the fluorescence filters DAPI-1160A and TRITC-A. The relative fluorescence intensity per cell was analysed from fluorescence micrographs using ImageJ.

Cell counting and mitochondrial metabolic activity. Cells were seeded in a 96-well plate at 7000 cells per well and incubated overnight. Cells were treated with **1** or **2** at 0.001, 0.05, 0.25, 0.5, 1, 5, 10 or 20 μM for 24 h. For cell counting, nuclei were labelled with Hoechst 33342 (1 μM) for 30 min at 37 °C, then cells were imaged using a fluorescence microscope (Leica DMI4000 B) at 10× magnification using the fluorescence filters DAPI-116A. Cell numbers were counted in ImageJ. To measure mitochondrial metabolic activity, cells were incubated with 0.5 mg mL^{-1} 3-(4,5-dimethylthiazol-2-yl)-2,5-diphenyltetrazolium Bromide (MTT, Sigma-Aldrich, 0.5 mg mL^{-1}) for 30 min at 37 °C. The medium was removed, and cells were lysed in DMSO (100 μL per well). Absorbance was measured using a plate reader (Tecan Infinite M1000) at 595 nm.

X-Ray crystallography. Crystals were cut with a razor to obtain regular aspect ratios and mounted on a 150 μm Mitogen mount using Paratone-N oil from Hampton research. Diffraction was carried out with a BRUKER APEX-II CCD diffractometer using graphite-monochromated Mo Kα1 radiation (λ = 0.71073 Å). Temperature was controlled at 80 K using an Oxford Cryosystems Cryostream 1000 open-flow cryostat. Unit cell determination was carried out at room temperature and redetermined after collection of a full 60 mm hemisphere at 80 K in 4 runs of 366 images each. Unit cell redetermination was carried out using the first 36 frames from each run, using reflections with $I/\sigma(I) \geq 8$. Data was integrated and scaled with the BRUKER APEX2 software package, using SAINT and SADABS for integration of images, and for determination of a multi-scan absorption correction respectively.[61,62] Structure was solved with dual-space methods *via* ShelXT in the Olex 2-1.5 graphical user interface.[63,64] Refinement was carried out on F^2 with a full least squares matrix using ShelXL.[65] Cycles of 20 iterations were used to produce a crystallographic model, and cycles of 200 were used to reach a minimum. Structures were checked with PLATON7 prior to submission.[66,67] Crystal structure figures were generated using Mercury and POV-Ray.[68]

3. Results and discussion

3.1 Synthesis of seminaphthofluorescein propargyl ethers

Pioneering work by Feng *et al.* indicated that both allyl ether and aliphatic substituents, installed on the xanthene oxygen and pendant carboxylic acid, were capable of inducing aggregation-induced emission behaviour in simple fluoresceins.[39] While no general structure/framework for the ACQ to AIE transition was established, we propose that dual functionalization of the xanthene oxygen and pendant acid with moieties possessing a degree of steric bulk may be a comprehensive strategy for the construction of AIE active xanthenes. Here we sought to expand the scope of this strategy *via* the synthetic modification of seminaphthofluoresceins, asymmetric benzannulated fluorescein derivatives known for their high Stokes shifts and ratiometric pH sensing capability.[43,44] Simple terminal alkynes (propargyl) were selected as the ideal substituent to both impart AIE characteristics and enable facile customization though click techniques. The side-by-side characterization of TPRP-SNAFL **1** and DPRP-SNAFL **2** additionally facilitated an investigation of the effect of a third substituent (installed in the 5 position on the lower ring) with respect to both solution state and aggregate properties.

Compounds **1** and **2** (represented in Scheme 1) were synthesized in a single step from their parent benzo[*c*]xanthenes, 5-carboxy-seminaphthofluorescein and seminaphthofluorescein. We have previously reported a rapid and economic synthesis of 5-carboxy-seminaphthofluorescein, the precursor to **1**.[69] The synthesis and characterization of the simple seminaphthofluorescein used to prepare **2** is detailed in the SI. Reaction of these benzo[*c*]xanthene starting materials with an excess of propargyl bromide yielded the fully substituted propargyl ethers TPRP-SNAFL **1** (tri-propargyl, derived from 5-carboxy-seminaphthofluorescein) and DPRP-SNAFL **2** (di-propargyl, derived from seminaphthofluorescein). Structural verification of compounds **1** and **2** was carried out by standard NMR and high-resolution mass spectrometry (see SI).

3.2 Solution optical properties

Compounds **1** and **2** displayed high solubility in various aprotic organic solvents including acetone, acetonitrile,

Table 1 Optical properties of seminaphthofluorescein propargyl ethers TPRP-SNAFL 1 and DPRP-SNAFL 2, dissolved (acetone) and in the aggregated (70% water/acetone) state

	TPRP-SNAFL							DPRP-SNAFL						
Solvent	λ_{abs}/nm	ε_λ/M^{-1} cm^{-1}	λ_{em}/nm	Stokes/nm	Φ_f	τ/ns	k_r/10^7 s^{-1}	λ_{abs}/nm	ε_λ/M^{-1} cm^{-1}	λ_{em}/nm	Stokes/nm	Φ_f	τ/ns	k_r/10^7 s^{-1}
Acetone	485	21 500	561 600	76	0.11 ± 0.01	2.1	5.2	483	21 800	552 589	69	0.14 ± 0.01	2.4	5.8
Water/acetone (f_w = 70 v/v%)	489 521	26 400 24 400	555	67	0.21 ± 0.02	2.8	7.5	485 518	29 600 28 000	549	64	0.32 ± 0.03	3.4	9.4

chloroform, dichloromethane, dimethyl sulfoxide, ethyl acetate, and tetrahydrofuran. Variation of solvent polarity within the range of selected aprotic organics induced only minor variations in absorbance and emission wavelengths (Fig. S22–S23 and S35–S36), as predicted by the absence of structural features associated with significant solvatochromism.[70,71] Acetone was selected as the model organic solvent to investigate the behaviour of both species in the dissolved state (Table 1). Absorbance in acetone appeared as a distinctive 'triplet' pattern, with maxima at 485 nm (ε = 21 500 M^{-1} cm^{-1}) for TPRP-SNAFL and 483 nm (ε = 21 800 M^{-1} cm^{-1}) for DPRP-SNAFL. Both the maximum absorbance wavelengths and extinction coefficients bore resemblance to the neutral 'naphthol' form of SNAFL (Table S1). The naphthol species, rather than the deprotonated red emitting naphtholate, is most relevant for comparison with derivatives fixed in a neutral state, including the SNAFL propargyl ethers. Immediately striking was the emission band broadness for both **1** and **2**, with full width half maximum (FWHM) values of 96 and 90 nm, respectively (SI – Fig. S48 and Table S2). The installation of both two and three propargyl ether substituents on the seminaphthofluorescein structure induced bathochromic shifts in emission from the parent compounds in the neutral forms, as illustrated in Fig. 1. In a broader context, the emission maximum of TPRP-SNAFL, at 560 nm, represented a 40 nm redshift from fluorescein.[4] Significantly, this shift in the emission band is expected to reduce overlap with biological fluorescence, by extension improving signal to noise and enabling use of the Cy3 filter for imaging. Further, compounds **1** and **2** mirrored their seminaphthofluorescein precursors with respect to Stokes shifts. At 76 nm in pure acetone, the Stokes shift of **1** (9 nm higher than that of **2**) was a remarkable 54 nm higher than that of fluorescein.[4] Attributed to the symmetry breaking nature of the benzo[*c*]xanthene structure, these high Stokes shifts are expected to reduce self-quenching and interference from excitation sources, collectively improving signal to noise ratios.[72–74]

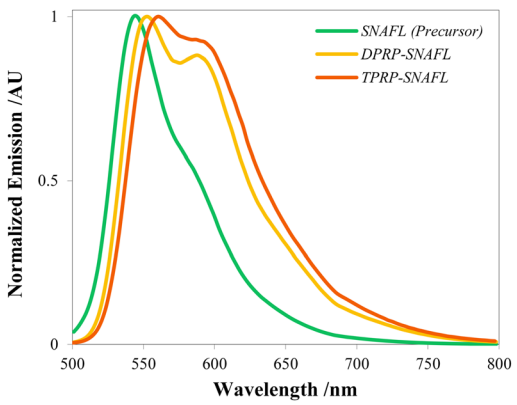

Fig. 1 Comparative emission spectra of carboxy-SNAFL (neutral form, pH 6 PBS buffer, λ_{ex} = 485 nm), DPRP-SNAFL **2** (dissolved, acetone, λ_{ex} = 485 nm), and TPRP-SNAFL **1** (dissolved, acetone, λ_{ex} = 485 nm).

The emission properties of DPRP-SNAFL and TPRP-SNAFL differed, an interesting departure from traditional xanthenes, in which the phenyl pendant moiety has little influence on the overall chromophore.[75] In line with this general rule, the spectral and photophysical properties of precursors seminaphthofluorescein and 5-carboxy-seminaphthofluorescein have been reported to be nearly identical.[43] Here, in contrast, the presence of a third propargyl ether substituent on the lower ring induced a 9 nm bathochromic shift in emission and 7 nm increase in Stokes shift. Both fluorophores were seen to have two emission maxima in organic solvents, with differences in the intensity of the lower energy peak. TPRP-SNAFL emitted at a maximum wavelength of 561 nm in acetone, with a substantial shoulder centred around 600 nm. In comparison, DPRP-SNAFL was seen to have two clearly defined emission peaks, at 552 and 589 nm. Relative quantum yields in acetone were calculated to be 0.11 for compound **1** and 0.14 for **2**. While the majority of xanthenes, including SNAFL, are essentially non-fluorescent in neutral organic solvents, the propargyl ether seminaphthofluoresceins possessed low-moderate brightness in acetone. The quantum yields of compounds **1** and **2** in acetone may be attributed to modification of the 2′ carboxylic acid of SNAFL, eliminating the ability of the species to undergo ring closure to a colourless, non-emissive structure.[4,76] In addition, functionalization of the xanthene oxygen eliminated the SNAFL protolytic equilibrium, rendering the compounds largely insensitive to pH.[77,78]

3.3 Aggregation-induced emission characteristics

A binary acetone/aqueous solvent system was employed to probe the potential AIE behaviour of compounds **1** and **2**. The virtual insolubility of the SNAFL propargyl ethers in water was

confirmed to ensure that the aqueous component was suitable to induce aggregation. TPRP-SNAFL **1** was investigated first in a sequence of binary solutions of varying aqueous fractions (f_w). Incredibly, even minor water fractions (<10% v/v) brought about clear changes in absorbance, fluorescence lifetimes, and emission intensity (Fig. 2). The impact of aggregation on absorption spectra was first examined with respect to TPRP-SNAFL, as seen in Fig. 2A. With higher aqueous fractions, the optical density of the primary band at 485 nm was increased alongside a minor redshift to 488 nm. Absorptivity was enhanced with increasing water fraction up to f_w = 70%, after which signal dropped rapidly (Fig. S26). This 'cutoff point', an exceptionally common feature of AIEgens, may be attributed to the formation of poorly dispersed aggregates not readily measured by solution-based techniques. The intensity of the band at 521 nm was more markedly increased, raising the extinction coefficient from 12 900 M^{-1} cm^{-1} in pure acetone to 24 400 M^{-1} cm^{-1} at f_w = 70%. Changes in the absorbance spectra of **2** imitated those of **1** (Fig. S27 and S28). A minor redshift and moderate increase in optical density of the primary 483 nm peak were observed, paired with a significant increase in absorptivity of the red edge (ε_{518} = 12 800 M^{-1} cm^{-1} → 28 000 M^{-1} cm^{-1}).

The progressive induction of aggregation was then investigated with respect to fluorescence emission. Remarkably, emission intensity for both species was doubled with the addition of only 10% water to the solvent system. As depicted in Fig. 2B, fluorescence emission progressively increased, reaching a maximum at a water fraction of 70%. When normalized to initial emission in pure acetone, final emission intensity at f_w = 70% was calculated to be improved by a factor of 3.5 for **1** and 3.7 for **2** (Fig. 2C). The quantum yield of TPRP-SNAFL at this aqueous fraction was 0.21 ($\Phi_{aggregated}/\Phi_{dissolved}$ = 1.9) while that of DPRP-SNAFL was 0.32 ($\Phi_{aggregated}/\Phi_{dissolved}$ = 2.3). The increase in aqueous fraction was accompanied by changes to emission wavelength and peak

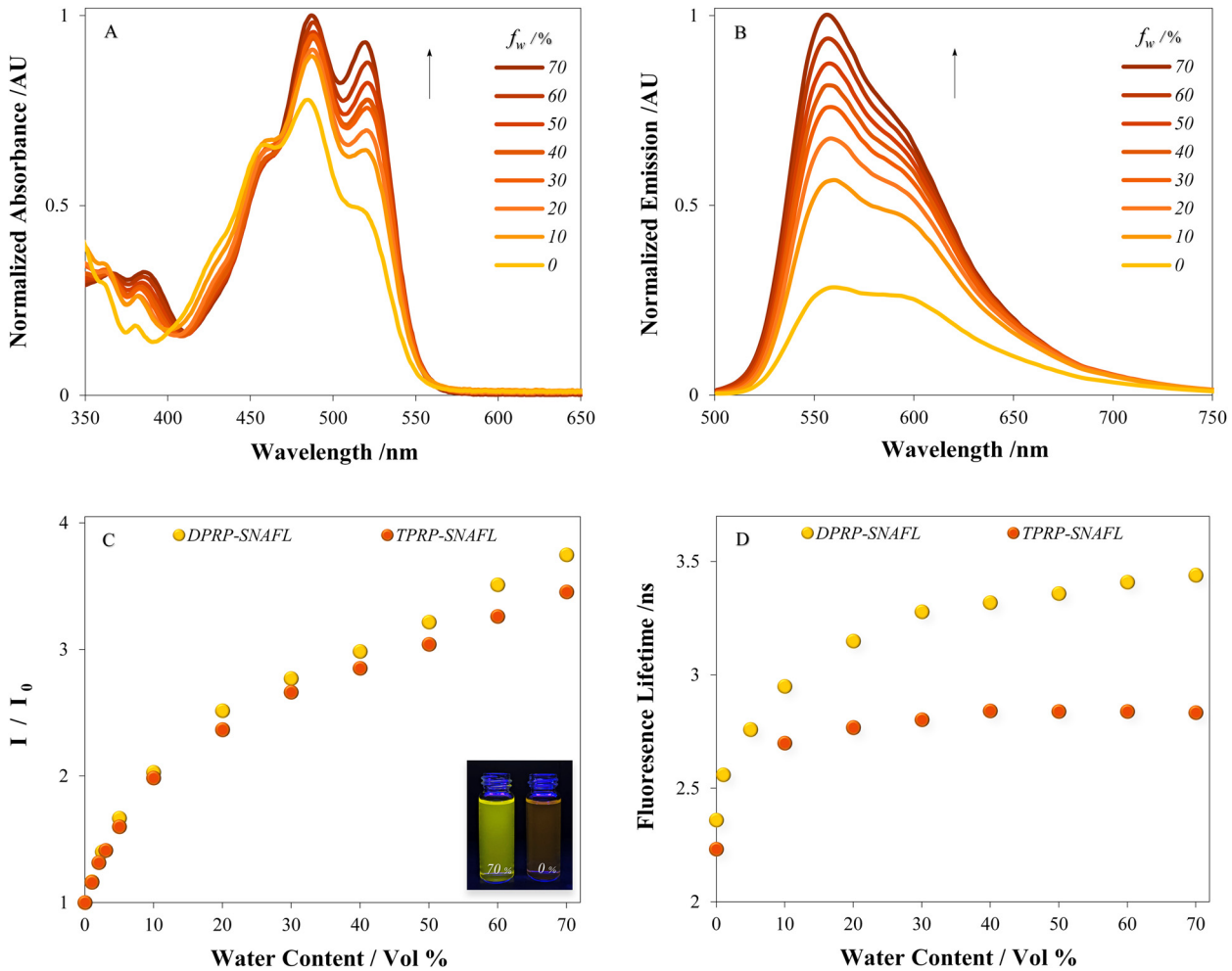

Fig. 2 (A) Normalized UV-Vis absorbance spectra of **1** (7.5 μM) in acetone/aqueous binary mixtures of varying water content (fraction by volume, f_w); (B) normalized fluorescence emission spectra of **1** (1.5 μM) in acetone/aqueous binary mixtures of varying water content; (C) relative fluorescence intensity of **1** and **2** (1.5 μM) with varying water fraction normalized to emission in pure acetone. Inset: Fluorescence photographs of 2 μM dissolved (f_w = 0%, acetone) and aggregated (water/acetone, f_w = 70%) DPRP-SNAFL under a 365 nm light source; (D) variation of fluorescence lifetimes of **1** and **2** corresponding to changes in water fraction (acetone/aqueous solvent system).

shape (Fig. S33 and S34). The characteristic broadness of the emission bands in the dissolved state was seen to progressively narrow with aggregation. The FWHM of TPRP-SNAFL emission was reduced to 78 nm while that of DPRP-SNAFL was calculated to be 72 nm. The significant reductions in FWHM, around 20 nm, corresponded primarily to decreases in the secondary/shoulder peaks in the 600 nm range. In addition, minor hypsochromic shifts in emission maxima occurred, totalling 6 nm for **1** and 3 nm for **2**. The aggregation-controlled modulation of brightness and emission wavelength was readily observed by illumination of the solutions, as illustrated in Fig. 2C (inset). Dim orange-yellow emission was seen in pure acetone, as suggested by the low calculated brightness for the dissolved state. The introduction of water to the solvent system markedly intensified emission and shifted colour to a yellow shade. Changes in fluorescence lifetimes were then traced for the SNAFL propargyl ethers (Fig. 2D). The lifetime of TPRP-SNAFL increased from 2.2 ns in pure acetone to a maximum of 2.8 ns at f_w = 70%. A significant jump in lifetime occurred between the pure organic and 10% water fraction, with a near plateau occurring thereafter. In contrast, DPRP-SNAFL underwent a gradual but striking increase in τ_f from 2.4 to 3.4 ns in the same range. These values were then utilized to estimate excited state decay rate constants ($k_r = \Phi_f/\tau_f$) for both luminogens. For TPRP-SNAFL, aggregation induced an increase in the radiative decay rate from 5.2×10^7 s^{-1} to 7.5×10^7 s^{-1}. Similarly, the formation of colloidal aggregates of DPRP-SNAFL increased k_r from 5.8×10^7 s^{-1} to 9.4×10^7 s^{-1}, consistent with the higher quantum yield. This observed increase in the radiative decay rate with the formation of aggregates, corresponding to a reduction in the non-radiative component k_{nr}, is a fundamental characteristic of AIE luminogens.[15,79,80]

The current range of AIE active species is diverse, with properties reflecting the breadth of structural and mechanistic variety. Early AIEgens, largely tetraphenylethylenes and siloles, were characterized by a rapid 'ON' response at aqueous fractions in the range of 60–90%.[13,81] The nearly undetectable quantum yields of these species in the dissolved state resulted in high degrees of brightness improvement, up to three digits in magnitude. The existing range of total emission enhancement factors (commonly defined as I_{final}/I_0 or $\Phi_{aggregate}/\Phi_{solution}$) spans orders of magnitude. Currently, no defined numerical threshold exists to separate AIE from the related category of aggregation-induced emission enhancement (AIEE/AEE). A central review by the Tang group describes AIE as a phenomenon in which the aggregates of a molecule have stronger emission than the dissolved (single molecule) species, indirectly emphasizing the lack of a clear distinction.[82] AIEE, characterized loosely by reasonable brightness in the dissolved state which is improved by the formation of aggregates, may be considered a minor subcategory of the broader AIE phenomenon. Considering these factors, we propose that compounds **1** and **2** may be appropriately described by either term until a numerical threshold dividing AIE and AIEE is established.

3.4 Water content sensing

In contrast to the vast majority of AIEgens which light up in a narrow window of aqueous composition, the observed water sensitivity of compounds **1** and **2** over the impressive range of ~1–70% f_w presents an interesting opportunity for the quantification of water content in organic solvents. The aqueous contamination of organic solvents remains a critical concern in the petrochemical industry and commercial scale synthesis, amongst others.[83] While the Karl Fisher titration and other classical electrochemical/electrophysical techniques are well established, optical methods are increasingly being sought as accessible alternatives.[83,84] As a result of the limited range of water response by existing AIEgens, these species have only found application in water sensing through solvatochromism (stemming from the common D–A structural motif).[85,86] In contrast, the SNAFL propargyl ethers demonstrated water sensing capability through simple emission enhancement and absorbance changes.

For both luminogens **1** and **2**, log–log plots of the emission ratio I/I_0 as a function of water fraction exhibited linear characteristics over a wide range of solution compositions. Compounds **1** and **2** demonstrated good linearity in the range of 1–70% (R^2 = 0.995 and 0.994, respectively; Fig. S45). Ideal response was determined to be in the 5–50% window for DPRP-SNAFL and 3–60% for TPRP-SNAFL, with identical correlation coefficients of 0.9991 (Fig. 3B). A concentration of 1.5 μM was utilized here to ensure that optical density did not exceed 0.1 AU. While not suited for trace analysis under 1%, compounds **1** and **2** offer the opportunity for quantification of water content over an unusual range of aqueous fractions. In addition, quantification by absorbance was seen to be possible. Monitoring of the ratio between the primary (483/485 nm) and aggregation associated (518/521 nm) absorbance bands revealed linearity with respect to the aqueous fraction f_w. The linear dynamic range was observed to be 10–70% for both TPRP-SNAFL and DPRP-SNAFL (R^2 = 0.992, Fig. S46). Ideal linearity was in the range of 20–70%, with correlation coefficients of 0.9975 for **1** and 0.9994 for **2** (Fig. 3A). The sensitivity of DPRP-SNAFL was seen to marginally exceed that of **1**, as suggested by comparative optical properties in the aggregate state.

3.5 Visualization of aggregates

To gain insights on the size, shape, and organization of the aggregates, the luminogens at high and low water fraction were investigated directly by fluorescence microscopy. Analysis of DPRP-SNAFL in an acetone solution containing trace water revealed the presence of aggregates, consistent with the optical response of the luminogens to low aqueous fractions. At this solution composition spherical particles averaging approximately 500 nm in diameter were seen to cluster into short chains (Fig. 4A). Imaging binary acetone/water solutions of high aqueous fraction (f_w = 70%) allowed for the simultaneous visualization of both the primary nanoaggregates and crystalline material (Fig. 4B). In contrast to the particles generated in primarily organic solution, the spherical aggregates were not seen to group into chains. A larger size distribution was noted,

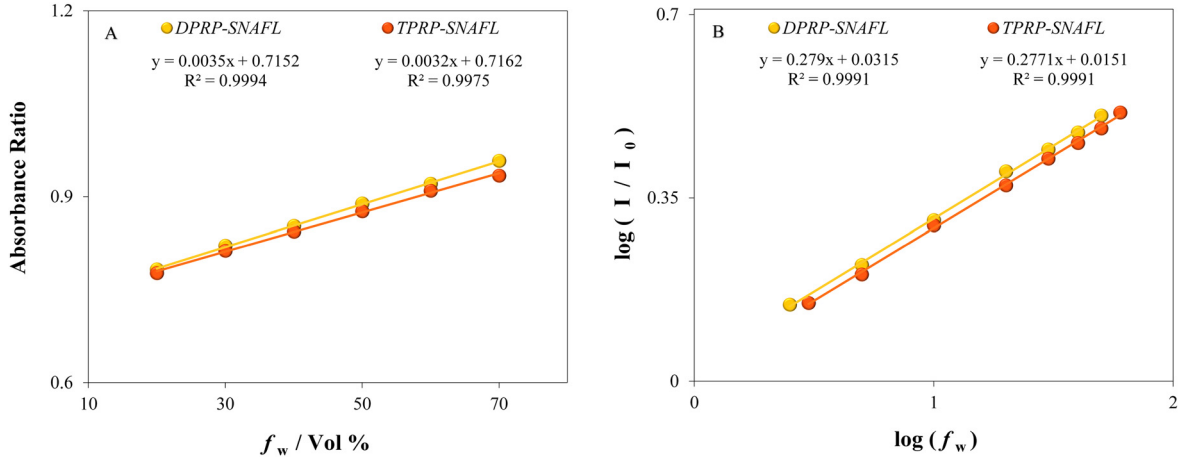

Fig. 3 Quantification of water content in acetone *via* (A) absorbance ratio (TPRP-SNAFL: 521/485 nm, DPRP-SNAFL: 518/483 nm); and (B) emission enhancement factor I/I_0.

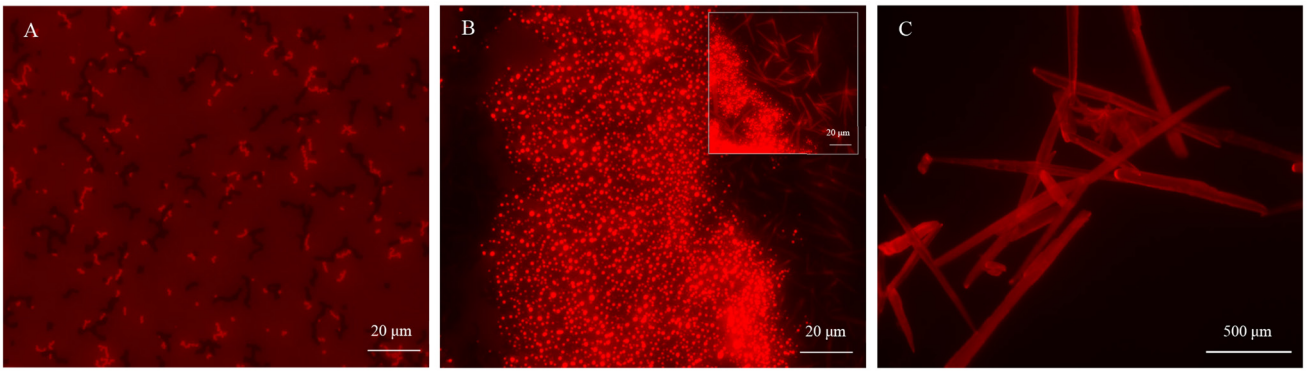

Fig. 4 Visualization of aggregates by fluorescence microscopy. Solutions of DPRP-SNAFL in (A) acetone containing trace water; (B) binary acetone/water mixture at 70% v/v. Inset: Co-existence of spherical particles and elongated rods at drying edge/solvent front; and (C) aged solution of TPRP-SNAFL acetone/water mixture (f_w = 70% v/v).

with visible nanoparticles in the range of 500 to 1000 nm. In addition to the spherical aggregates, elongated needle-like objects (~20 μm in length) were observed along the drying edge of the solution. These structures had a striking resemblance to single crystals of TPRP-SNAFL grown from an acetone/water system (Fig. 4C). The coexistence of the primary aggregate morphology with these needles suggested the presence of small single crystals in solutions of >70% f_w when not carefully protected from evaporation. Atomic force microscopy (AFM) was utilized as a high-resolution complement to fluorescence images of the aggregates in solution. AFM analysis of the 70% v/v solution uncovered the presence of small (average 25 nm) nanoparticles. Intriguingly, the dominant large spherical particles observed by fluorescence microscopy were seen to be clusters of the ~25 nm particles, confirming this as the primary aggregate size and morphology (Fig. S76–S78).

3.6 Modulating aggregation – solvent effects

To further probe the aggregation process, the effects of various solvents were investigated. While water is often employed as the near universal non-solvent for AIEgens, we questioned the use of organic alternatives and the possibility of impacts on aggregation process. Hexanes was identified as a rare organic solvent in which the luminogens exhibited sparing solubility. TPRP-SNAFL was prepared in a series of binary solutions of acetone/hexanes, analogous to previous experiments with the acetone/water solvent system. Increasing the fraction of hexanes in solution resulted in the rapid decay of emission intensity (Fig. S42). A plot of I/I_0 with respect to the volume percentage of hexanes was highly linear in the range of 0–60%, after which point a more marked drop in intensity occurred (Fig. S44). Throughout the $f_{hexanes}$ range, the changes in emission intensity were not coupled with any observable variation in the emission profile or wavelength maximum (Fig. S43). Significantly, the consistency in optical properties indicated that no organized structures were present in solution. Rather, it was likely that hexanes induced true precipitation, from which the aggregates were not dispersed and suitable for solution state measurements.

Unusual behaviour of the luminogens in alcohols was identified while assessing solubility. While the compounds

Table 2 Spectral and photophysical properties of seminaphthofluorescein propargyl ethers 1 and 2 aggregated in selected alcohols

	TPRP-SNAFL					DPRP-SNAFL				
Solvent	λ_{abs}/nm	λ_{em}/nm	Φ_f	τ/ns	$k_r/10^7$ s^{-1}	λ_{abs}/nm	λ_{em}/nm	Φ_f	τ/ns	$k_r/10^7$ s^{-1}
Methanol	487	555	0.28 ± 0.03	3.1	9.4	485	549	0.30 ± 0.03	3.7	8.1
Ethanol	490	555	0.23 ± 0.03	3.2	7.2	487	549	0.32 ± 0.03	3.7	8.7

were visually soluble at low concentrations, optical properties suggested the dominance of aggregates (Table 2). A pure alcohol solvent system successfully generated well dispersed, highly emissive aggregates without a co-solvent, as was required when utilizing water to induce aggregation. In methanol the quantum yield of TPRP-SNAFL was calculated to be 0.28, with a fluorescence lifetime of 3.1 ns. These values, along with the high radiative rate constant (9.4×10^7 s^{-1}), exceeded those of **1** in the 70% aqueous acetone/water solvent system (Φ = 0.21). The same held true for DPRP-SNAFL, with a nearly identical quantum yield of 0.30 and a 3.7 ns fluorescence lifetime. In ethanol, the quantum yield of **1** was slightly diminished, while **2** remained within error. This divergence may be attributed to differences in polarity and solubility between the SNAFL propargyl ethers. The enhanced optical properties in alcohols are likely a reflection of the lack of an aprotic/good solvent for the compounds, maximizing aggregation. In addition, the initial non-solvent (MQ water) was exchanged with PBS buffer to examine the effect of salts on aggregation of the luminogens. An analysis of optical properties in a PBS/acetone solution (f_w = 70%) confirmed that the buffer had no discernable impact on the aggregates (Fig. S38 and Table S3).

3.7 Crystal structure analysis

Crystal structure analysis remains a gold standard tool for mechanistic insights on aggregation-induced emission processes. The formation of H-type aggregates, in which π–π interactions are prevalent and significantly suppress fluorescence, is a common mechanism of ACQ for highly conjugated, planar compounds.[7,9] ACQ of fluoresceins is thought to be the result of π stacking of xanthene faces. Intermolecular hydrogen bonding between the ketone oxygen and hydroxyl groups of neighbouring xanthenes is expected to facilitate this close contact and the dominance of non-radiative decay pathways. However, the complexity of obtaining high quality single crystals of fluoresceins has remained an obstacle to investigations in this area, which have as a result relied on P-XRD and other techniques.[87,88] Analysis of the readily grown XRD quality of xanthene AIEgens is potentially a complementary pathway to understanding the ACQ of simple fluoresceins. X-Ray quality single crystals of TPRP-SNAFL (triclinic with space group $P\bar{1}$) were grown from an acetone/water solvent system for this purpose.

In the crystal structure analysis of their AIE luminogens, Feng *et al.* most significantly noted a staggering of xanthene faces, attributed to steric repulsion imparted by the allyl and short aliphatic chain substituents.[39] While the elimination of the likely mechanism of ACQ for xanthenes (close face-to-face π interactions) is significant, this feature alone cannot account for the emission enhancement as proposed by Feng. As a manifestation of the interest in this apparent ACQ to AIE transformation, recent computational work has sought to elucidate a possible mechanism.[89] In contrast to early/classic AIEgens, the factors contributing to the relatively low solution state fluorescence of the fluorescein and seminaphthofluorescein luminogens are not immediately apparent. An analysis of the neutral form of fluorescein provides an important window into the relevant non-radiative decay pathways.[90] Quenching of this neutral species, analogous to the substituted AIEgens, was proposed to result from interaction of the nπ* and ππ* excited states. Upon excitation to the bright ππ* (S_1) state, non-radiative decay is enhanced by vibronic coupling with the close lying 'dark' nπ* (S_2) state, a process known as the proximity effect. The authors of this computational study additionally present an alternative pathway in which relaxation through a conical intersection to the nπ* state occurs, followed by non-radiative decay. For these compounds in the solid state, calculations revealed both reduced rotation between the xanthene and lower benzene ring and a beneficial change in energy for the nπ* and ππ* excited states. The increase in energy of the nπ* state, resulting in the placement of the bright ππ* state as S_1, was credited to intermolecular hydrogen bonding. The complete ACQ to AIE transition was attributed to three factors: the elimination of π stacking interactions, restriction of rotation, and the reduction of non-radiative decay resulting from the nπ* state *via* intermolecular hydrogen bonding.[89]

We observed a similar offset of the xanthene π system in the crystal structure of TPRP-SNAFL, with intermolecular distances in the range of 3.4 Å with respect to aromatic faces (Fig. S66). Viewing a select xanthene π system and its nearest neighbouring aromatic unit top-down, through the rings, shows no signs of face-to-face overlap or relevant short contacts (interatomic distance < vdW radii). The structure revealed a highly twisted compound, a feature which is closely tied to rotation based non-radiative decay. The average torsion angle was calculated to be 68.2° between the upper xanthene unit and pendant phenyl ring (Fig. S68). A variety of significant hydrogen bonding interactions were observed (Fig. 5), including between propargyl – methylene hydrogens and propargyl ≡C–H to the xanthene C=O:, as well as ≡C–H···:O=C dimers between propargyl groups across inversion centers, which leads to expression of an inversion symmetric, $R_2^2$14 supramolecular dimer motif. The noted hydrogen intermolecular hydrogen bonds are proposed to contribute to a fixed conformation with

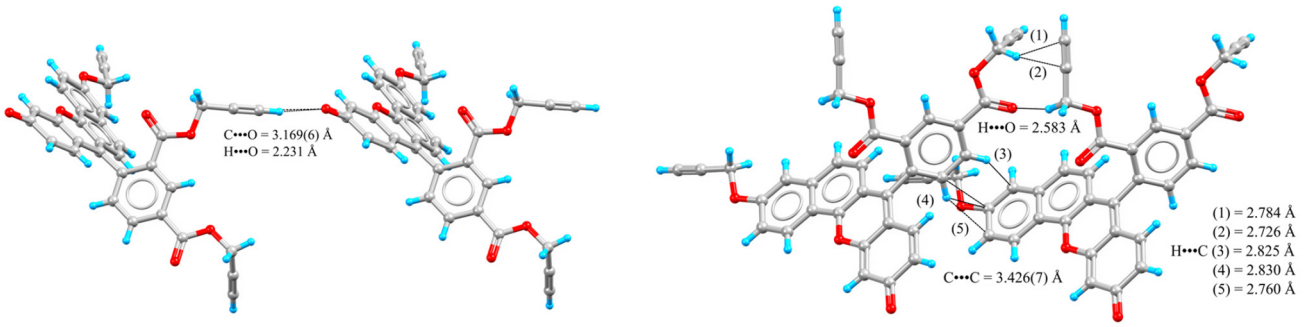

Fig. 5 X-Ray crystal structure of TPRP-SNAFL, illustrating intermolecular interactions for significant dimers. All interatomic distances between rendered molecules shown as dashed lines and atoms rendered with a ball-and-stick model.

reduced rotational motion. Taken together, the recent computational work and our crystal structure analysis point towards a lesser known mechanism of AIE, restriction of access to the dark state (RADS).[89,91,92] This effect is associated with the limited number of AIEgens possessing a heteroatom and closely intertwined with restriction of rotation/motion.

3.8 Intracellular imaging

The pure compounds, in their aggregate form, were tested in human microglia to evaluate the potential for live cell imaging applications. These cells hold a crucial role in maintaining brain homeostasis by constantly surveying the brain, removing debris from degraded proteins or remnants of damaged neural cells and engaging in inflammatory and other mechanisms.[93,94] Microglia can also contribute to neurodegeneration when hyperactivated by producing excessive proinflammatory cytokines and chemokines. Similarly, inadequately active non-homeostatic microglia such as those in the aging brain are incapable of removing accumulating biological aggregates.[58]

TPRP-SNAFL and DPRP-SNAFL were easily internalized by human microglia and uptake was observed in a time and concentration-dependent manner. Intracellular fluorescence from the aggregates was detectable in live microglia within 5 minutes, with maximal intensity achieved between 30 and 45 minutes for both compounds (Fig. 6A). The luminogens showed comparable intracellular fluorescence intensities, also seen from concentration-dependent measurements in cell lysates after 24 h (Fig. 6B). Despite the absence of organelle targeting moieties, the aggregates were mainly localized in mitochondria, as shown by co-labelling with MitoTracker Deep Red (Fig. 7 and Fig. S85). Decreased mitochondrial metabolic activity, along with decreased cell numbers, was only significant at concentrations above 10 μM. Thus, the use of the luminogens at lower concentrations should not impair mitochondria activity or cell viability (Fig. S82 and S83).

The conditions of TPRP-SNAFL and DPRP-SNAFL fluorescence in mitochondria were further investigated by assessing dependence on mitochondria membrane potential ($\Delta\Psi_m$). The aggregates were compared to tetramethylrhodamine ethyl

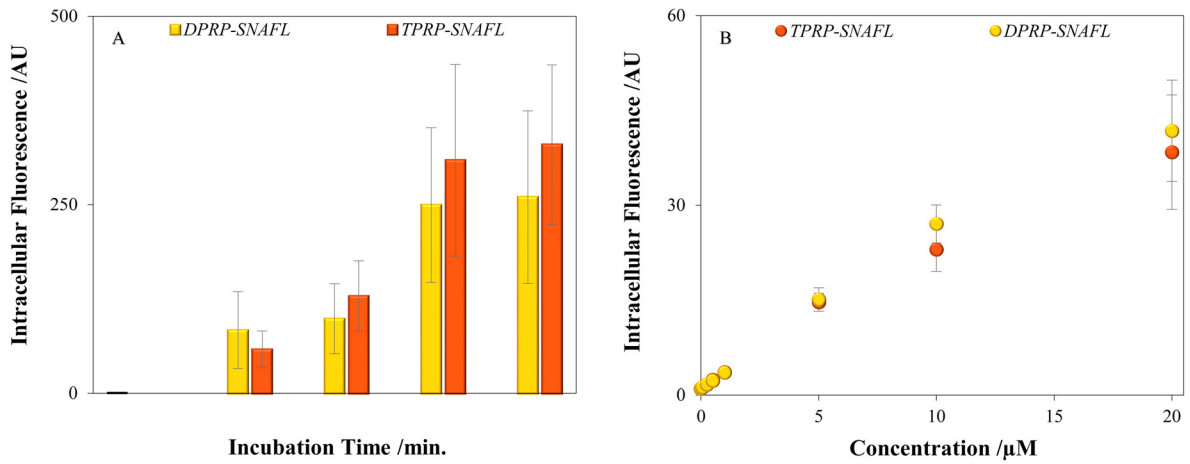

Fig. 6 Concentration and time dependent increase of intracellular luminogen fluorescence in human HMC3 microglia cells. (A) Average level of intracellular fluorescence per cell ± standard error from at least 75 cells treated with TPRP-SNAFL or DPRP-SNAFL at 1 μM, from three independent experiments. (B) Fluorescence from lysates of microglia treated with 0.001, 0.05, 0.25, 0.5, 1, 5, 10 and 20 μM 1 or 2 for 24 h. Untreated cells served as control.

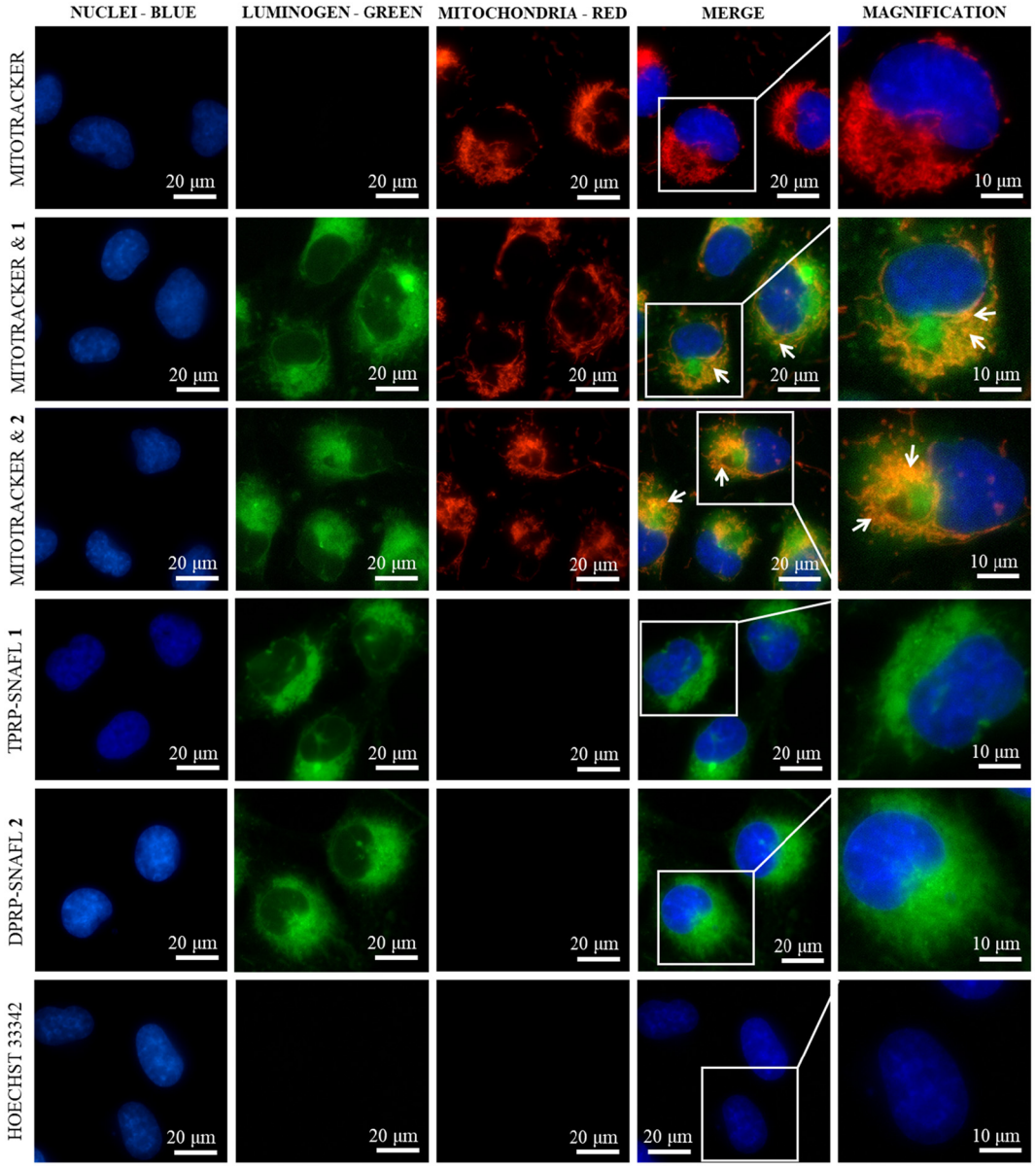

Fig. 7 Co-labelling of mitochondria with TPRP-SNAFL **1** and DPRP-SNAFL **2** in human HMC3 microglia cells. Fluorescence micrographs of microglia cells treated with **1** or **2** (green, 1 μM) for 30 min in HBSS. Nuclei (blue) were labelled with Hoechst 33342. Mitochondria (red) were labelled with MitoTracker Deep Red Cells were washed and imaged using a fluorescence microscope with the UV, Cy3 and Cy5 filters (DAPI-1160A, Semrock, ex: 387 nm, em: 447 nm; TRITC-A, Semrock, ex: 542 nm, em: 620 nm; CY5-404A, Semrock, ex: 628 nm em: 692 nm). White arrowheads indicate sites of overlap between mitochondria and the luminogen.

ester perchlorate (TMRE), a cationic fluorescent probe utilized to detect changes in mitochondrial membrane potential.[95–97] Treatment of the cells with carbonyl cyanide-*p*-trifluoromethoxyphenylhydrazone (FCCP), an uncoupler that decreases mitochondrial membrane potential by transporting protons across the mitochondrial membrane, was seen to significantly decrease intracellular TMRE fluorescence as expected. The same protocol did not dissipate TPRP-SNAFL and DPRP-SNAFL fluorescence to the same extent, indicating that presence of the aggregates in mitochondria was not critically dependent on mitochondria membrane potential (Fig. S80 and S81).

Mitochondria specific probes are nearly universally cationic, with partitioning in the organelle according to the Nernst equation.[97–100] A limited number of fluorophores which fall outside this structural framework have been reported to target mitochondria, though relatively little is understood about the physical processes behind their selective accumulation.[101–103] Neutral mitochondria-targeted species are highly sought after for their largely potential-independent nature, allowing both accumulation and retention in depolarized (unhealthy or fixed) mitochondria. Both initial localization of the neutral luminogens TPRP-SNAFL and DPRP-SNAFL in mitochondria and their

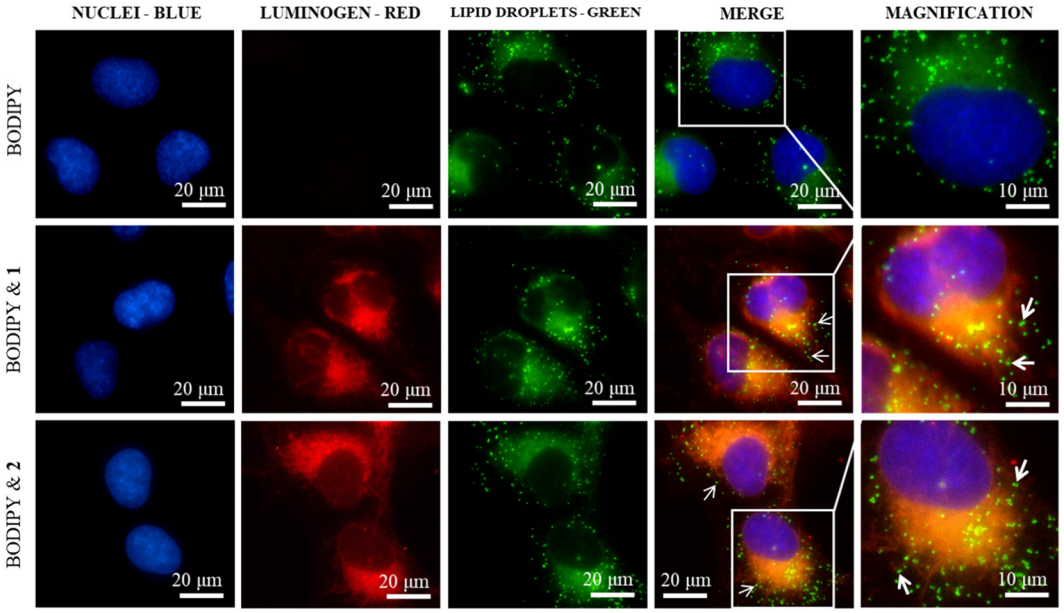

Fig. 8 Co-labelling of lipid droplets with TPRP-SNAFL **1** and DPRP-SNAFL **2** in human HMC3 microglia cells. Fluorescence micrographs of microglia cells treated with **1** or **2** (red, 1 μM) for 30 min in HBSS. Nuclei (blue) were labelled with Hoechst 33342. Lipid droplets (green) were labelled with BODIPY 493/503. Cells were washed and imaged using a fluorescence microscope with the UV, Cy3 and Cy5 filters (DAPI-1160A, Semrock, ex: 387 nm, em: 447 nm; TRITC-A, Semrock, ex: 542 nm, em: 620 nm; CY5-404A, Semrock, ex: 628 nm em: 692 nm). White arrows indicate sites of close proximity between lipid droplets and the luminogen.

retention in the organelle are unlikely to be directly tied to membrane potential, as confirmed by the limited optical response to membrane depolarization though FCCP treatment and cell fixation (Fig. S86).

Beyond classic CuAAC click chemistry, the functionality of the luminogens provides an opportunity for future development as a platform for ultra long-term imaging. Recent work has demonstrated fluorophores possessing non-activated alkynes can undergo coupling with thiols (thiol–yne 'click') in reactive oxygen species (ROS) rich mitochondria of cancer cells.[104] Intracellular covalent fixation/immobilization of fluorophores is a well established method to facilitate stable long term organelle imaging and serves most notably as the basis of the ubiquitous MitoTracker series.[105–109] While the radical thiol–yne reaction of luminogens **1** and **2** is expected to be limited with respect to the non-cancerous HMC3 cell line, the abundance of endogenous thiols in the inner mitochondrial membrane coupled with the key role of the organelle in ROS production points to a degree of coupling.[110–112]

The imaging utility of the aggregates was further shown by co-labelling lipid droplets (LD), dynamic organelles known to interact with mitochondria.[55,57] The fatty acid breakdown in mitochondria occurs *via* beta oxidation and serves as one of the energy sources and constituents of plasma membrane. The role of lipid droplets goes far beyond an energy source, as they are signalling platforms participating in cellular communication.[113–115] As depicted in Fig. 8, the luminogen labelled mitochondria did not significantly co-localize with the BODIPY493/503 labelled lipid droplets but the two organelles were observed in close proximity.

4. Conclusion

We have developed a new class of xanthene luminogens uniting aggregation-induced emission, click customizability, and the capacity for organelle bioimaging. Built on the framework of seminaphthofluorescein (SNAFL), these compounds signify the first major advancement in AIE active fluoresceins since their discovery in 2020 while simultaneously addressing the persistent limitations of conventional xanthenes (high energy emission, low Stokes shifts). While the solution state was characterized by low intensity orange-yellow emission, protic non-solvents triggered changes to optical properties consistent with the major hallmarks of AIE. The yellow emitting molecular aggregates, visualized directly by fluorescence microscopy, exhibited improved brightness in both pure alcohols and binary organic–aqueous solutions (Φ = 0.21–0.28 for TPRP-SNAFL **1**, Φ = 0.30–0.32 for DPRP-SNAFL **2**). The gradual and controlled rise in both absorptivity and quantum yield over a remarkably broad range of organic–aqueous solution compositions facilitated the optical sensing of water content. Monitoring of an absorbance ratio enabled quantification in the range of 20–70% f_w for both luminogens while sensing *via* emission ratio was possible over a larger span of aqueous fractions (3–60% and 5–50% for **1** and **2**, respectively).

The translation of AIE active fluoresceins to bioimaging was realized here for the first time. Collectively, these studies show that fluorescent aggregates of TPRP-SNAFL and DPRP-SNAFL are versatile tools for imaging mitochondria, assessing mitochondria–LD interactions, and for the development of functional assays in living microglia and other cells. The aggregates

are promising to be studied in models of pathology using human organoids to investigate mitochondrial morphology and movements related to cell functions dependent on mitochondria. In the broader context of AIEgen development, TPRP-SNAFL and DPRP-SNAFL set the stage for the rapid development of functional xanthene aggregates for specialized biological applications.

Author contributions

Conceptualization: L. M., A. K., D. M. Investigations: L. M., I. Z., I. S. Visualization: L. M., I. Z. Writing – original draft, review and editing: L. M., I. Z., D. S. B., A. K., D. M. Supervision: D. S. B., A. K., D. M. Funding acquisition: D. S. B., A. K., D. M.

Conflicts of interest

Authors declare no conflicts of interest.

Data availability

All other relevant data generated and analyzed during this study are included in this article and its supplementary information (SI). Supplementary information is available. See DOI: https://doi.org/10.1039/d5nr04595a.

CCDC 2496456 (**1**) contains the supplementary crystallographic data for this paper.[116]

Acknowledgements

LM and AK acknowledge AFM services provided by the Microscopy and Imaging Lab at McGill University and Dr S. Sewall for access to instrumentation. DSB acknowledges the Natural Sciences and Engineering Research Council of Canada (grant number 2019-20456). AK would like to thank the Natural Sciences and Engineering Research Council of Canada (grant number RGPIN-2023-03565), and New Frontiers in Research Fund – Exploration, Canada (grant number NFRFE-2022-00356) for financial assistance. DM thanks the Natural Sciences and Engineering Research Council of Canada (grant number RGPIN 2020-07011) for funding.

References

1 L. D. Lavis and R. T. Raines, *ACS Chem. Biol.*, 2014, **9**, 855–866.
2 J. E. Whitaker, R. P. Haugland, D. Ryan, P. C. Hewitt, R. P. Haugland and F. G. Prendergast, *Anal. Biochem.*, 1992, **207**, 267–279.
3 M. Beija, C. A. M. Afonso and J. M. G. Martinho, *Chem. Soc. Rev.*, 2009, **38**, 2410–2433.
4 R. Sjöback, J. Nygren and M. Kubista, *Spectrochim. Acta, Part A*, 1995, **51**, L7–L21.
5 X.-F. Zhang, J. Zhang and L. Liu, *J. Fluoresc.*, 2014, **24**, 819–826.
6 G. v. Bünau, *Bunsen-Ges. Phys. Chem., Ber.*, 1970, **74**, 1294–1295.
7 M. K. Bera, P. Pal and S. Malik, *J. Mater. Chem. C*, 2020, **8**, 788–802.
8 S. Ma, S. Du, G. Pan, S. Dai, B. Xu and W. Tian, *Aggregate*, 2021, **2**, e96.
9 J. B. Birks, *Photophysics of Aromatic Molecules*, Wiley-Interscience, 1970.
10 S. A. Meredith, Y. Kusunoki, S. D. Connell, K. Morigaki, S. D. Evans and P. G. Adams, *J. Phys. Chem. B*, 2023, **127**, 1715–1727.
11 J. T. Cirulis, B. C. Strasser, J. A. Scott and G. M. Ross, *Cytometry, Part A*, 2012, **81**, 618–626.
12 J. C. Waters, in *Methods in Cell Biology*, ed. G. Sluder and D. E. Wolf, Academic Press, 2013, vol. 114, pp. 125–150.
13 J. Luo, Z. Xie, J. W. Y. Lam, L. Cheng, H. Chen, C. Qiu, H. S. Kwok, X. Zhan, Y. Liu, D. Zhu and B. Z. Tang, *Chem. Commun.*, 2001, 1740–1741.
14 F. Würthner, *Angew. Chem., Int. Ed.*, 2020, **59**, 14192–14196.
15 S. Suzuki, S. Sasaki, A. S. Sairi, R. Iwai, B. Z. Tang and G.-i. Konishi, *Angew. Chem., Int. Ed.*, 2020, **59**, 9856–9867.
16 Z. He, C. Ke and B. Z. Tang, *ACS Omega*, 2018, **3**, 3267–3277.
17 J. Mei, N. L. C. Leung, R. T. K. Kwok, J. W. Y. Lam and B. Z. Tang, *Chem. Rev.*, 2015, **115**, 11718–11940.
18 X. Cai and B. Liu, *Angew. Chem., Int. Ed.*, 2020, **59**, 9868–9886.
19 C. Zhu, R. T. K. Kwok, J. W. Y. Lam and B. Z. Tang, *ACS Appl. Bio Mater.*, 2018, **1**, 1768–1786.
20 L. Yan, Y. Zhang, B. Xu and W. Tian, *Nanoscale*, 2016, **8**, 2471–2487.
21 W.-J. Wang, Z.-Y. Xin, X. Su, L. Hao, Z. Qiu, K. Li, Y. Luo, X.-M. Cai, J. Zhang, P. Alam, J. Feng, S. Wang, Z. Zhao and B. Z. Tang, *ACS Nano*, 2025, **19**, 281–306.
22 M. Huang, A. K. S. Camara, D. F. Stowe, F. Qi and D. A. Beard, *Ann. Biomed. Eng.*, 2007, **35**, 1276–1285.
23 J. Qian and B. Z. Tang, *Chem*, 2017, **3**, 56–91.
24 R. A. J. Smith, C. M. Porteous, A. M. Gane and M. P. Murphy, *Proc. Natl. Acad. Sci. U. S. A.*, 2003, **100**, 5407–5412.
25 C. W. T. Leung, Y. Hong, S. Chen, E. Zhao, J. W. Y. Lam and B. Z. Tang, *J. Am. Chem. Soc.*, 2013, **135**, 62–65.
26 X. Zhao, Y. Chen, G. Niu, D. Gu, J. Wang, Y. Cao, Y. Yin, X. Li, D. Ding, R. Xi and M. Meng, *ACS Appl. Mater. Interfaces*, 2019, **11**, 13134–13139.
27 Y. Zhao, R. T. K. Kwok, J. W. Y. Lam and B. Z. Tang, *Nanoscale*, 2016, **8**, 12520–12523.
28 Z. Liu, Z. Jiang, M. Yan and X. Wang, *Front. Chem.*, 2019, **7**, 712.
29 M. M. Islam, Z. Hu, Q. Wang, C. Redshaw and X. Feng, *Mater. Chem. Front.*, 2019, **3**, 762–781.

30 Z. Zhao, B. He and B. Z. Tang, *Chem. Sci.*, 2015, **6**, 5347–5365.
31 D. Yan, Q. Wu, D. Wang and B. Z. Tang, *Angew. Chem., Int. Ed.*, 2021, **60**, 15724–15742.
32 Z. Gui, S. Gong and G. Feng, *Anal. Chem.*, 2024, **96**, 6724–6729.
33 S. Zhang, S. Gong, J. Hong, J. Zhang and G. Feng, *Anal. Chem.*, 2025, **97**, 2318–2325.
34 M. Mathivanan, B. Tharmalingam, O. Anitha, T. Thiruppathiraja, S. Lakshmipathi, J. Grzegorz Małecki and B. Murugesapandian, *J. Mol. Liq.*, 2023, **382**, 121845.
35 V. K. Singh, R. Prasad, B. Koch, S. H. Hasan and M. Dubey, *New J. Chem.*, 2017, **41**, 5114–5120.
36 Z. Ma, Z. Wang, X. Meng, Z. Ma, Z. Xu, Y. Ma and X. Jia, *Angew. Chem., Int. Ed.*, 2016, **55**, 519–522.
37 L.-L. Yang, H. Wang, J. Zhang, B. Wu, Q. Li, J.-Y. Chen, A. L. Tang, J. W. Y. Lam, Z. Zhao, S. Yang and B. Z. Tang, *Nat. Commun.*, 2024, **15**, 999.
38 S. Kamino, Y. Horio, S. Komeda, K. Minoura, H. Ichikawa, J. Horigome, A. Tatsumi, S. Kaji, T. Yamaguchi, Y. Usami, S. Hirota, S. Enomoto and Y. Fujita, *Chem. Commun.*, 2010, **46**, 9013–9015.
39 S. Feng, S. Gong and G. Feng, *Chem. Commun.*, 2020, **56**, 2511–2513.
40 A. Pinto, A. Llanos, R. M. Gomila, A. Frontera and L. Rodríguez, *Inorg. Chem.*, 2023, **62**, 7131–7140.
41 Z. Khan and N. Sekar, *Dyes Pigm.*, 2023, **208**, 110735.
42 S. Kamino and M. Uchiyama, *Org. Biomol. Chem.*, 2023, **21**, 2458–2471.
43 J. E. Whitaker, R. P. Haugland and F. G. Prendergast, *Anal. Biochem.*, 1991, **194**, 330–344.
44 E. Azuma, N. Nakamura, K. Kuramochi, T. Sasamori, N. Tokitoh, I. Sagami and K. Tsubaki, *J. Org. Chem.*, 2012, **77**, 3492–3500.
45 P. Hammershøj, E. Thyrhaug, P. Harris, P. K. Ek, T. L. Andresen and M. H. Clausen, *Tetrahedron Lett.*, 2017, **58**, 1611–1615.
46 M. Sibrian-Vazquez, J. O. Escobedo, M. Lowry, F. R. Fronczek and R. M. Strongin, *J. Am. Chem. Soc.*, 2012, **134**, 10502–10508.
47 H. Zhu, J. Fan, J. Du and X. Peng, *Acc. Chem. Res.*, 2016, **49**, 2115–2126.
48 W. Xu, Z. Zeng, J.-H. Jiang, Y.-T. Chang and L. Yuan, *Angew. Chem., Int. Ed.*, 2016, **55**, 13658–13699.
49 P. Gao, W. Pan, N. Li and B. Tang, *Chem. Sci.*, 2019, **10**, 6035–6071.
50 H. Crawford, M. Dimitriadi, J. Bassin, M. T. Cook, T. F. Abelha and J. Calvo-Castro, *Chem. – Eur. J.*, 2022, **28**, e202202366.
51 H. Wang, B. Fang, B. Peng, L. Wang, Y. Xue, H. Bai, S. Lu, N. H. Voelcker, L. Li, L. Fu and W. Huang, *Front. Chem.*, 2021, **9**, 683220.
52 Y. Ma, R. Song and C. Duan, *Front. Immunol.*, 2025, **16**, 1542369.
53 P. Cassina, E. Miquel, L. Martínez-Palma and A. Cassina, *Neuroscience*, 2025, **567**, 227–234.
54 D. S. Kathiresan, R. Balasubramani, K. Marudhachalam, P. Jaiswal, N. Ramesh, S. G. Sureshbabu, V. M. Puthamohan and M. Vijayan, *Mol. Neurobiol.*, 2025, **62**, 6827–6855.
55 Y. Xie, W. Sun, A. Han, X. Zhou, S. Zhang, C. Shen, Y. Xie, C. Wang and N. Xie, *Front. Mol. Neurosci.*, 2025, **17**, 1527013.
56 L. Zhang, Y. Zhou, Z. Yang, L. Jiang, X. Yan, W. Zhu, Y. Shen, B. Wang, J. Li and J. Song, *J. Neuroinflammation*, 2025, **22**, 7.
57 M. E. Traetta, H. A. Vecchiarelli and M.-È. Tremblay, *J. Neurochem.*, 2025, **169**, e16259.
58 R. Gao, Y. Gao, W. Su and R. Wang, *Aging Dis.*, 2025, **17**, 91–113.
59 K. T. P. McElroy, *J. Am. Chem. Soc.*, 1894, **16**, 618–620.
60 E. V. Ivanov, V. K. Abrosimov and E. Y. Lebedeva, *J. Solution Chem.*, 2008, **37**, 1261–1270.
61 G. M. Sheldrick, SADABS, *Program for Empirical Adsorption Correction of Area Detector Data*, University of Göttingen, Germany, 1996..
62 G. Sheldrick, *Acta Crystallogr., Sect. A: Found. Crystallogr.*, 2008, **64**, 112–122.
63 G. Sheldrick, *Acta Crystallogr., Sect. A: Found. Crystallogr.*, 2015, **71**, 3–8.
64 O. V. Dolomanov, L. J. Bourhis, R. J. Gildea, J. A. K. Howard and H. Puschmann, *J. Appl. Crystallogr.*, 2009, **42**, 339–341.
65 G. Sheldrick, *Acta Crystallogr., Sect. C: Struct. Chem.*, 2015, **71**, 3–8.
66 A. L. Spek, *J. Appl. Crystallogr.*, 2003, **36**, 7–13.
67 A. Spek, *Acta Crystallogr., Sect. D: Biol. Crystallogr.*, 2009, **65**, 148–155.
68 C. F. Macrae, I. Sovago, S. J. Cottrell, P. T. A. Galek, P. McCabe, E. Pidcock, M. Platings, G. P. Shields, J. S. Stevens, M. Towler and P. A. Wood, *J. Appl. Crystallogr.*, 2020, **53**, 226–235.
69 L. McKay, N. Joma, D. Maysinger and A. Kakkar, *J. Mater. Chem. B*, 2025, **13**, 11790–11808.
70 A. S. Klymchenko, *Acc. Chem. Res.*, 2017, **50**, 366–375.
71 C. Reichardt, *Chem. Rev.*, 1994, **94**, 2319–2358.
72 T.-B. Ren, W. Xu, W. Zhang, X.-X. Zhang, Z.-Y. Wang, Z. Xiang, L. Yuan and X.-B. Zhang, *J. Am. Chem. Soc.*, 2018, **140**, 7716–7722.
73 H. Liu, G. Jiang, G. Ke, T.-B. Ren and L. Yuan, *ChemPhotoChem*, 2024, **8**, e202300277.
74 J. Yang, Z. Xu, L. Yu, B. Wang, R. Hu, J. Tang, J. Lv, H. Xiao, X. Tan, G. Wang, J.-X. Li, Y. Liu, P.-L. Shao and B. Zhang, *Angew. Chem., Int. Ed.*, 2024, **63**, e202318800.
75 Y. Urano, M. Kamiya, K. Kanda, T. Ueno, K. Hirose and T. Nagano, *J. Am. Chem. Soc.*, 2005, **127**, 4888–4894.
76 N. Klonis and W. H. Sawyer, *J. Fluoresc.*, 1996, **6**, 147–157.
77 N. O. McHedlov-Petrossyan, T. A. Cheipesh, S. V. Shekhovtsov, A. N. Redko, V. I. Rybachenko, I. V. Omelchenko and O. V. Shishkin, *Spectrochim. Acta, Part A*, 2015, **150**, 151–161.
78 Z.-G. Zhao, T. Shen and H.-J. Xu, *Spectrochim. Acta, Part A*, 1989, **45**, 1113–1116.

79 Q. Peng and Z. Shuai, *Aggregate*, 2021, **2**, e91.
80 Y. Chen, J. W. Y. Lam, R. T. K. Kwok, B. Liu and B. Z. Tang, *Mater. Horiz.*, 2019, **6**, 428–433.
81 Y. Dong, J. W. Y. Lam, A. Qin, J. Liu, Z. Li, B. Z. Tang, J. Sun and H. S. Kwok, *Appl. Phys. Lett.*, 2007, **91**, 011111.
82 Z. Zhao, H. Zhang, J. W. Y. Lam and B. Z. Tang, *Angew. Chem., Int. Ed.*, 2020, **59**, 9888–9907.
83 H. S. Jung, P. Verwilst, W. Y. Kim and J. S. Kim, *Chem. Soc. Rev.*, 2016, **45**, 1242–1256.
84 P. Rivera-Quintero, G. S. Patience, N. A. Patience, D. C. Boffito, X. Banquy and D. Schieppati, *Can. J. Chem. Eng.*, 2024, **102**, 2980–2997.
85 W. Chen, Z. Zhang, X. Li, H. Ågren and J. Su, *RSC Adv.*, 2015, **5**, 12191–12201.
86 Y. Zhang, D. Li, Y. Li and J. Yu, *Chem. Sci.*, 2014, **5**, 2710–2716.
87 M. Tremayne, B. M. Kariuki and K. D. M. Harris, *Angew. Chem., Int. Ed. Engl.*, 1997, **36**, 770–772.
88 M. Arhangelskis, M. D. Eddleston, D. G. Reid, G. M. Day, D.-K. Bučar, A. J. Morris and W. Jones, *Chem. – Eur. J.*, 2016, **22**, 10065–10073.
89 G. Jiang, J. Liu and P. Zhou, *J. Phys. Chem. A*, 2023, **127**, 5193–5201.
90 P. Zhou, Z. Tang, P. Li and J. Liu, *J. Phys. Chem. Lett.*, 2021, **12**, 6478–6485.
91 Y. Tu, J. Liu, H. Zhang, Q. Peng, J. W. Y. Lam and B. Z. Tang, *Angew. Chem., Int. Ed.*, 2019, **58**, 14911–14914.
92 S. Huang, J. Ding, A. Bi, K. Yu and W. Zeng, *Adv. Opt. Mater.*, 2021, **9**, 2100832.
93 M. Pereira-Iglesias, J. Maldonado-Teixido, A. Melero, J. Piriz, E. Galea, R. M. Ransohoff and A. Sierra, *Nat. Neurosci.*, 2025, **28**, 15–23.
94 F.-D. Shi and V. W. Yong, *Science*, 2025, **388**, eadx0043.
95 R. C. Scaduto Jr. and L. W. Grotyohann, *Biophys. J.*, 1999, **76**, 469–477.
96 L. C. Crowley, M. E. Christensen and N. J. Waterhouse, *Cold Spring Harb. Protoc.*, 2016, **2016**, 1092–1096.
97 O. Tovar-Ferrero, J. Rubio, A. Zorzano, G. Martínez-Corrales and M. Liesa, *EMBO J.*, 2025, **44**, 7334–7345.
98 J. J. Lemasters and V. K. Ramshesh, in *Methods in Cell Biology*, Academic Press, 2007, vol. 80, pp. 283–295.
99 H. Wang, B. Fang, B. Peng, L. Wang, Y. Xue, H. Bai, S. Lu, N. H. Voelcker, L. Li, L. Fu and W. Huang, *Front. Chem.*, 2021, **9**, 683220.
100 L. D. Zorova, V. A. Popkov, E. Y. Plotnikov, D. N. Silachev, I. B. Pevzner, S. S. Jankauskas, V. A. Babenko, S. D. Zorov, A. V. Balakireva, M. Juhaszova, S. J. Sollott and D. B. Zorov, *Anal. Biochem.*, 2018, **552**, 50–59.
101 I. Ferraboschi, J. Ovčar, K. V. Vygranenko, S. Yu, A. Minervino, A. Wrzosek, A. Szewczyk, R. Rozza, A. Magistrato, K. D. Belfield, D. T. Gryko, L. Grisanti and C. Sissa, *Org. Biomol. Chem.*, 2024, **22**, 5886–5890.
102 C. Ripoll, P. Herrero-Foncubierta, V. Puente-Muñoz, M. C. Gonzalez-Garcia, D. Miguel, S. Resa, J. M. Paredes, M. J. Ruedas-Rama, E. Garcia-Fernandez, M. Roldan, S. Rocha, H. De Keersmaecker, J. Hofkens, M. Martin, J. M. Cuerva and A. Orte, *Pharmaceutics*, 2021, **13**, 254.
103 A. A. Vidyakina, S. A. Silonov, A. Y. Ivanov, E. A. Shpakova, M. D. Kim, E. P. Podolskaya, A. S. Gladchuk, I. A. Balova, S. Bräse and N. A. Danilkina, *J. Mater. Chem. B*, 2025, **13**, 10525–10535.
104 J. Köckenberger, I. Klemt, C. Sauer, A. Arkhypov, V. Reshetnikov, A. Mokhir and M. R. Heinrich, *Chem. – Eur. J.*, 2023, **29**, e202301340.
105 B. Chazotte, *Cold Spring Harb. Protoc.*, 2011, **2011**, 990–992.
106 K. Neikirk, A. G. Marshall, B. Kula, N. Smith, S. LeBlanc and A. Hinton, *Eur. J. Cell Biol.*, 2023, **102**, 151371.
107 X. Zhang, Q. Sun, Z. Huang, L. Huang and Y. Xiao, *J. Mater. Chem. B*, 2019, **7**, 2749–2758.
108 W. Meng, R. Chen, Q. Jang, K. Ma, D. Li, H. Xiao, W. Chi, C. Zeng and W. Shu, *Coord. Chem. Rev.*, 2025, **529**, 216456.
109 Y. Miao, Y. Tian and D. Ye, *Chem. Soc. Rev.*, 2025, **54**, 11624–11658.
110 J. Dan Dunn, L. A. J. Alvarez, X. Zhang and T. Soldati, *Redox Biol.*, 2015, **6**, 472–485.
111 M. Minozzi, A. Monesi, D. Nanni, P. Spagnolo, N. Marchetti and A. Massi, *J. Org. Chem.*, 2011, **76**, 450–459.
112 E. Cadenas and K. J. A. Davies, *Free Radicals Biol. Med.*, 2000, **29**, 222–230.
113 K. Mallick, S. Paul, S. Banerjee and S. Banerjee, *Neuroscience*, 2024, **549**, 13–23.
114 R. W. Klemm and P. Carvalho, *Annu. Rev. Cell Dev. Biol.*, 2024, **40**, 143–168.
115 L. Enkler and A. Spang, *FEBS Lett.*, 2024, **598**, 1235–1251.
116 CCDC 2496456: Experimental Crystal Structure Determination, 2026, DOI: 10.5517/ccdc.csd.cc2psrv3.